Sensors & Actuators: B. Chemical 361 (2022) 131694

Contents lists available at ScienceDirect

Sensors and Actuators: B. Chemical

journal homepage: www.elsevier.com/locate/snb

Influence of the test-chamber shape on the performance of conductometric gas sensors

L. Parellada-Monreal [a,b], G.G. Mandayo [a,b,*], A. Martín-Mayor [c], I. Souto-Canteli [c], M. Mounir Bou-Ali [c]

[a] CEIT-Basque Research and Technology Alliance (BRTA), Manuel Lardizábal 15, 20018 Donostia-San Sebastián, Spain
[b] Universidad de Navarra, Tecnun, Manuel Lardizábal 13, 20018 Donostia-San Sebastián, Spain
[c] Faculty of Engineering, Mechanical and Industrial Production, Mondragon Unibertsitatea, Loramendi 4, 20500 Mondragon, Gipuzkoa, Spain

ARTICLE INFO

Keywords:
Computational fluid dynamics (CFD)
Conductometric gas sensor
Gas flow
Chamber-position influence

ABSTRACT

In this article, CFD simulations results are presented as a key tool to the comprehension of the target gas concentration evolution in a test chamber, at different working conditions. The simulation results are compared with the experimental data, which shows a qualitative good correlation with the evolution of the concentration gradient detected. The experiments were carried out using an aluminum gas test chamber, where a WO_3 based conductometric sensor is introduced. The results demonstrate how the response time is dependent on the sensor working conditions. Analyzing the CFD and experimental results, some assumptions for this behavior are proposed.

The WO_3 sensor needs a Pt heating element, which is heated up to 300 °C. As the response is highly temperature-dependent, the temperature distribution on the sensor surface was measured by an IR thermographic camera. The simulation results show that the temperature distribution matches with those obtained experimentally. To validate the model, a mesh and time step convergence study was also implemented.

1. Introduction

Chemical low-cost sensors, and among them, conductometric gas sensors, are a widely researched area because of their numerous applications, ranging from dangerous gas detection for security purposes to electronic noses for food quality assessment. New materials, such as innovative forms of the traditional metal oxides, carbon-based nanostructures [1,2] or metal-oxide frameworks (MOFs) [3] predominantly capture the attention of the researchers. But the performance of metal oxide gas sensors can also be affected by the conditions under which the detection happens. Two of the most relevant parameters are the temperature of the material during detection and the target gas flow. The way the flow reaches the sensor surface is important for the velocity of the sensor response. When the experiments to characterize gas sensors are carried out, the position of the gas inlet and outlet in the sensor chamber and the magnitude of the gas flow have to be considered to know the evolution of the concentration gradient at the surface of the sensing material because the sensor response time can be affected. Furthermore, the sensor can be the origin of convective flows because the high temperature of several hundred degrees needed on the sensor surface to detect gas. In this context, flow simulations can help designing better experimental procedures and further understand the underlying dynamics of the gas diffusion mechanisms.

There have been several attempts to take advantage of simulation procedures to optimize the gas sensing conditions. Annanouch et al. [4] found a good correlation between the numerical results that give the analyte concentration and the sensor response in two different shapes of test chambers, in a similar way to Lopez et al. [5]. Both references are good examples of the utility of simulations to analyze the influence of the shape of the test chamber and the position of the sensor and its response. Niyat et al. [6] propose a method to simulate the active layer of the sensor, as well as including the temperature and the gas flow inside the chamber for a tin oxide/reduced graphene oxide conductometric sensor to detect NO_2. Although the model still shows some inaccuracies, it is a promising approach for the development of different active layers and sensor configurations.

This research work analyzes the influence of the sensor position in the test chamber and compares experimental results obtained with

* Corresponding author at: CEIT-Basque Research and Technology Alliance (BRTA), Manuel Lardizábal 15, 20018 Donostia-San Sebastián, Spain.
E-mail address: ggmandayo@ceit.es (G.G. Mandayo).

https://doi.org/10.1016/j.snb.2022.131694
Received 8 September 2021; Received in revised form 9 February 2022; Accepted 9 March 2022
Available online 12 March 2022

sensors fabricated on alumina substrates using computational flow dynamic (CFD) simulations. The comparison between numerical and experimental results is used to determine the real response time of the sensor.

2. Methodology

2.1. Experimental methodology

Gas tests with conductometric sensors were carried out by means of electrical measurements performed inside a cylindrical sealed aluminum chamber (Fig. 1a)) with a volume of 1.1 l. The sensor was plugged into a Digi-Key Electronics connector (ECC04DKWN-S1723), as shown in Fig. 1b) and thanks to the pressure contact, no bonding was needed. To prove the effectiveness of the positioning of the sensor, the connector and the sensor were supported on a stainless-steel part, as shown in Fig. 1c) to ensure that the sensor was kept at the center of the chamber facing the gas inlet for the "middle" position.

A schematic layout of the set-up is shown in Fig. 2. Feed-through connections in the chamber were used to control the heater temperature and measure the conductivity of the sensor. A constant voltage of 3 V was applied between the IDT electrodes, so intensity measurements were achieved through a Keithley 2000 Multimeter connected via General Purpose Interface Bus (GPIB) to the computer where a Labview© program acquired the data. The power consumption of the Pt heating element was doubly calibrated with a thermographic camera and a Pt100 resistor, so the heater was power controlled by a programmable voltage source (AMREL PPS-1326). The atmosphere inside the chamber was controlled by means of mass flow controllers (MFCs) from Bronkhorst Hi-Tech, which allows a maximum flow of 400 standard cubic centimeters per minute (sccm) and were monitored through a dynamic data exchange (DDE) communication via Labview©. The NO_2 gas was taken from a certified bottle (Air Liquide) of 50 ppm mixed with synthetic air. The response of a WO_3 based sensor was monitored at 300 °C for 5 ppm of NO_2.

The sensor was fabricated on a 1×2 cm^2 double-polished alumina substrate, where a Pt heater was patterned at the backside by photolithography followed by DC sputtering in an Edwards ESM 100 system and 1 mm^2 of WO_3 sensing layer was deposited on the top side of the alumina substrate by photolithography followed by RF sputtering in an argon (Ar) atmosphere. The details of the fabrication process are given in reference [7].

The response of the devices, SR, to the oxidizing gas NO_2, is defined as:

$$SR = R_{gas}/R_{air} = G_{air}/G_{gas} \quad (1)$$

where R_{air} is the resistance of the sensor in air, and R_{gas} represents the sensor resistance in the presence of the gas. The response time (T90) will be defined as the time required for the sensor to reach 90% of the maximum response after 30 min of exposure.

The sensor response was measured at four experimental conditions that make the situation change on the sensor surface. Four combinations of flow (200 and 400 sccm) and position (height of the sensor inside the chamber: at the bottom and at 64 mm) were tested. The summary of the four cases can be found in Table 1.

2.2. Numerical methodology

A brief description of the overall numerical method is given in this section. SCDM 2019 R3© was used as a preprocessor for creating the geometries models. The surface and volume mesh of the fluid domain were formed using ICEM CFD©. The completed mesh was imported to the respective numerical solver, ANSYS FLUENT©, where the simulation setup of a model was implemented. The simulation setup includes essential steps such as assigning the fluid properties, boundary conditions and numerical schemes for the model. At the end of the simulation setup, the fluid model consists of two mediums (fluid and solid) where the heat transfer affects the fluid flow.

2.2.1. Computational domain

The fluid domain was extracted from the original inner mixing chamber geometry and inner inlet/outlet valves geometries. The computational domain chamber has two different inner diameters. The bottom inner diameter is 78 mm and the upper inner diameter is 90 mm. The total height is 150 mm. The inlets and outlets have two different inner diameters of 5.7 mm and 6.2 mm. Fig. 3 shows the entire fluid domain and the sensor assembly. The simulations of the sensor behavior and the experimental measurements have been performed placing the sensor at two different heights (called "bottom position" and "middle position"). The first position is at the bottom of the chamber and the second one is at a height of 64 mm, as shown in Fig. 3.

2.2.2. Computational mesh

The computational domain of the mixing chamber was constructed of non-uniformly spaced structured tetrahedral finite volume cells using the pre-processor module ICEM. Afterward, the tetrahedral cells were converted to polyhedral cells in ANSYS Fluent, keeping the same values of the aspect ratio while reducing the number of elements, thus keeping at a low pace the computational time-cost relation. The mesh of the entire computational fluid domain is shown below in Fig. 4.

Prism layers around the sensor assembly wall were added to resolve more efficiently the boundary layer. In concordance with the turbulence model used and its requirements [8], a value $y+ \sim 1$ (non-dimensional distance from the wall to the first cell) was used. To maintain the $y+$ value in this range, the first prism layer must be placed at a height of

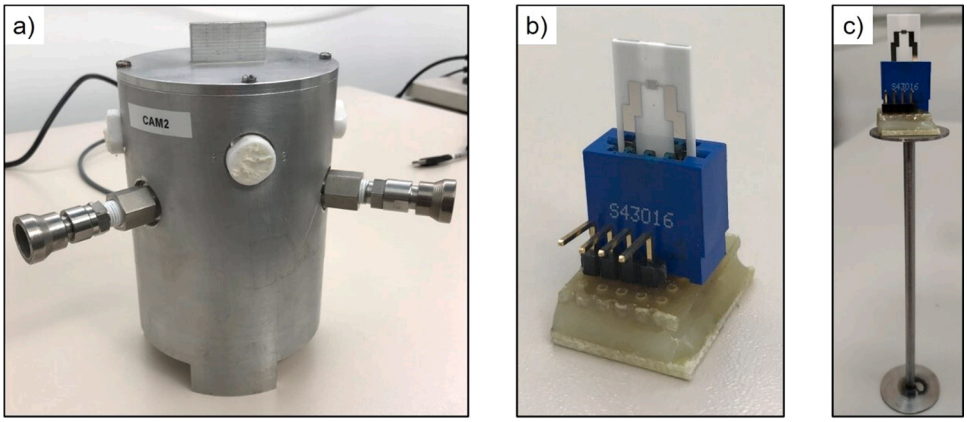

Fig. 1. a) Cylindrical sealed stainless-steel chamber with a volume of 0.86 l, b) connector for the sensor contacts and c) connector on a stainless steel base.

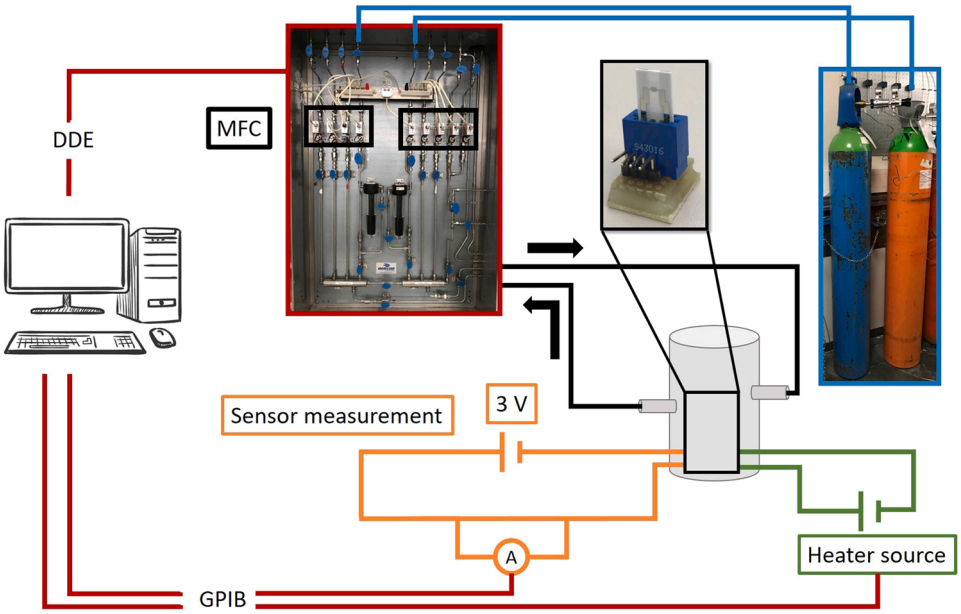

Fig. 2. Schematic layout of the set-up used for the electrical measurements.

Table 1
Experimental conditions in terms of gas flow and sensor height inside the chamber.

	Height (mm)	Flow (sccm)
CASE I	0	200
CASE II	0	400
CASE III	64	200
CASE IV	64	400

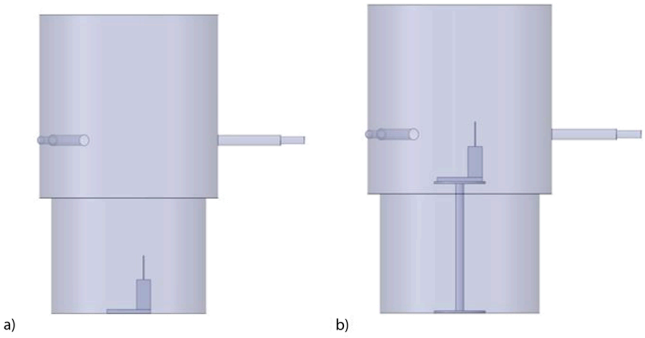

Fig. 3. Simulation fluid domain different height positions of the chip body a) sensor at the bottom position and b) sensor at the middle position.

0.005 mm. To achieve a prism layer total thickness of 0.1 mm, 10 prism layers have been used with a growth ratio of 1.15.

Three meshes of different resolutions have been created for the initial mesh resolution sensibility study. This is one of the main steps in a CFD analysis to make sure that the solution of the problem is independent of the mesh resolution. The mesh resolution used, where a mesh with 0.27 million cells, with 0.54 million cells (Fig. 4) and with 1 million cells.

2.2.3. Solver setup

A finite volume method (FVM) based numerical fluid flow solution methodology was used to solve the Navier-Stokes equations in the absence of reaction-transport equations and external body forces. These equations solve the laws of conservation of mass, momentum and energy that govern fluid mechanics. For unsteady and incompressible flows are

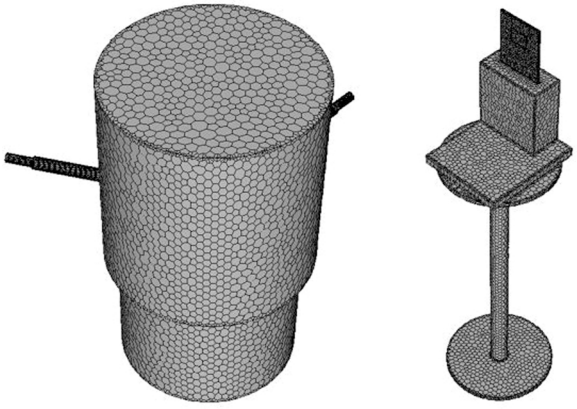

Fig. 4. Computational mesh of the fluid domain.

written as follows:

$$\frac{\partial \rho}{\partial t} + \nabla\left(\rho \vec{V}\right) = 0 \tag{1}$$

$$\rho \frac{\partial \vec{V}}{\partial t} + \rho\left(\nabla \vec{V}\right)\cdot \vec{V} = -\nabla P + \rho \vec{g} + \nabla(\mu \nabla \vec{V}) \tag{2}$$

$$\frac{\partial(\rho h)}{\partial t} + \nabla\left(\rho \vec{V} h\right) = \nabla\left[\left(K_{eff} \nabla T\right) - \left(\sum_i h_i \vec{J_i}\right)\right] \tag{3}$$

Where ρ is the mixture density, $\vec{V}$ is the velocity vector field, P is the static pressure, $\vec{g}$ is the gravitational vector, μ the dynamic viscosity, h represents the enthalpy, K_{eff} is the effective conductivity defined as $k + k_t$, where k is the thermal conductivity and k_t is the thermal turbulent conductivity (defined according to the turbulence model used) and T the temperature.

$\vec{J_i}$ is the diffusion flux of species i, that represents the fluid transport equations in binary mixtures in presence of temperature gradients and is applied for turbulent flows [9].

$$\overrightarrow{J_i} = -\rho D_i \nabla c_i - \frac{\mu_t}{Sc_t}\nabla c_i - D_{T,i}\frac{\nabla T}{T} \quad (4)$$

Where D_i is the molecular diffusion coefficient for the species i in the mixture, c is the mass fraction, $Sc_t$is the turbulent Schmidt number ($\frac{\mu_t}{\rho D_t}$ where μ_t is the turbulent viscosity and D_t is the turbulent diffusivity) and $D_T$is the thermodiffusion coefficient. The simulations were conducted under the SST (shear stress transport) $k-w$ turbulence model described by Menter [11].

A coupled unsteady flow solver (pressure-based coupled algorithm) was used. So for discretization, the coupled scheme was used for pressure-velocity coupling, and the second-order up-wind differencing scheme was used for the pressure interpolation, momentum (fluid flow), and species transport equations. Ideal gas laws were assumed for both the density and viscosity and the rest of the fluid properties were assumed to be constant for all simulations, which were conducted in presence of gravity. The convergence criterion was also set to 10^{-6} for the residuals of species and continuity to attain high numerical accuracy.

2.2.4. Boundary conditions

Velocity inlet boundary conditions were used to define the fluid stream velocities and mass fraction of the species of interest at the inlet boundary. The net transport of species at the inlet consisted of both convection and diffusion components. The convection component was specified with a mass fraction of $7.94{\cdot}10^{-6}$ of NO_2 in air, which corresponds to a concentration of 5 ppm of NO_2 in air. The diffusion component, however, was not specified a priori as it depends on the gradient of the computed species at the inlet. The specified inlet velocity for each fluid stream also ranged from 0.265 m/s and 0.424 m/s, corresponding to a flow rate of 200 sccm and 400 sccm.

Atmospheric pressure outlet boundary condition was applied to the outlet of the geometry, allowing the outflow value of pressure to atmospheric.

A No-slip boundary condition was imposed at all the wall boundaries. The chamber walls were set as a 14 mm thick aluminum wall with a heat transfer coefficient of 15 $W/m^2{\cdot}K$, which represents natural convention to a free steam at a 298.16 K. The sensor chip is set as a coupled ceramic material, with two different zones defined: the gas-sensitive material zone (WO_3 sensing layer area), where the NO_2 concentration will be evaluated, and the heat source zone, that represents the hottest area of the heating Pt resistor used in the sensor, where a temperature of 573 K is reached. This is a platinum 200 nm think integrated circuit. These two zones are at the same position but on different sides of the sensor chip as is illustrated in Fig. 5.

All material properties are summarized in Table 2 and Table 3. Furthermore, the fluid properties of the gases (air and NO_2) (Table 2) and the solid material used (Table 3) are shown.

Table 2
Properties for different fluids at 20 °C and atmospheric pressure.

Fluid	Density (kg/m^3)	Thermal Conductivity (W/m·K)	Viscosity (kg/m·s)	Molecular Weight (kg/kmol)	Molecular diffusion coefficient (m^2/s) [10]
Air	1.225	0.0242	$1.7894{\cdot}10^{-5}$	28.966	$0.1436\ 10^{-4}$
NO_2	1.449	0.0454	$1.72{\cdot}10^{-5}$	46.055	

Table 3
Properties for different solids at 20 °C.

Solid	Density (kg/m^3)	Specific Heat (J/kg·K)	Thermal Conductivity (W/m·K)
Alumina (Al_sO_3)	2719	571	202.4
Coorstek® ADS - 996 Ceramic	3880	871	26.6
Platinium	21,450	130	71.6

3. Results and discussion

The result and discussion section are divided into two different parts: in the first one the numerical results obtained from the simulations are presented and in the second one, key experimental results are compared to the numerical results.

3.1. Model validation

For the model validation, some steps were taken. First of all, a mesh convergence study was made to ensure the results are independent of the mesh. Secondly, it was verified that the time step used for the unsteady study was small enough to obtain a reliable result. Then it was confirmed that the steady-state and the unsteady simulations converged to the same results. Finally, using experimental images of a thermal camera, the experimental temperature map was compared with the numerical ones, for the thermal model validation.

3.1.1. Mesh convergence study

Three meshes of different resolutions were created to achieve a mesh convergence study. A steady-state simulation of the Case III was used to reduce computational time. The output parameters compared are summarized in Table 4.

It was confirmed that the results for the meshes used are almost constant even for the one with fewer elements. In addition, the wall y + parameter is below the maximum acceptable (wall y + = 3) value for all the cases. However, to ensure the quality of the results, the second mesh with more elements was used for the development of the work.

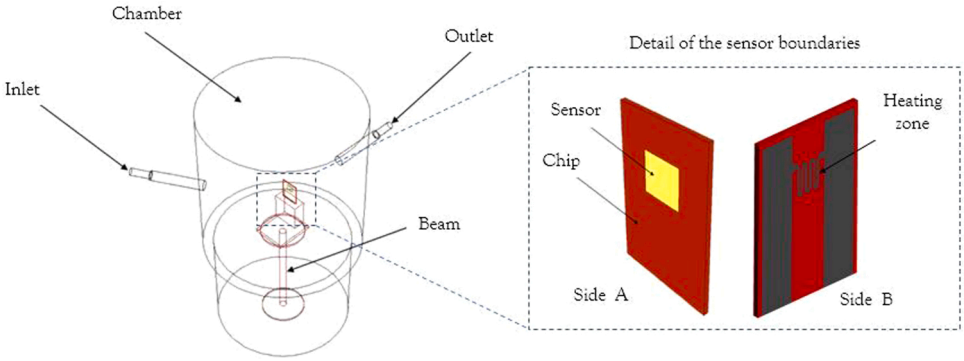

Fig. 5. Detail of the model, where sensing area and Pt resistor platinum circuit is shown.

Table 4
Mesh convergence parameters.

Mesh convergence			
	Reference values	Variation respect Reference value %	
Number of cells	1,081,893	≈ 50%	≈ 25%
Outlet velocity [m/s]	0.27	> 0.3%	> 0.4%
Outlet NO_2 Mass fraction	$7.94{\cdot}10^{-6}$	> 0.1%	> 0.1%
Mass fraction NO_2 in chamber	$7.94{\cdot}10^{-6}$	> 0.01%	> 0.01%
Mass fraction NO_2 on sensor	$7.32{\cdot}10^{-6}$	> 0.15%	> 0.15%
Temperature in chamber[K]	302.90	> 0.15%	> 0.15%
Temperature on sensor [K]	571.68	> 0.1%	> 0.1%
Wall y+	0.12	59%	110%

3.1.2. Time step convergence study

Time step size was calculated using CFL (Courant-Friedrichs-Lewy) criteria. The CFL condition expresses that the distance the information travels during the time-step length within the mesh must be lower than the distance between mesh elements. In other words, information from a given cell or mesh element must propagate only to its immediate neighbors. This is expressed by the next formula: CFL $= \frac{u \cdot \Delta t}{\Delta x}$ where u is the characteristic velocity of the problem, Δt the time step size and Δx the minimum mesh size. CFL must be 1 or less to ensure the correct convergence of the problem. The minimum mesh cell size was set to 1 mm, so being $\Delta x = 1mm$ and our characteristic velocity 0.26 m/s, a time step size of $3.77{\cdot}10^{-3}$ s will be used.

To make a time step convergence study, a lower time step size of $1.8{\cdot}10^{-3}$ was also simulated, to ensure that zones with smaller cell size (as the boundary layer) are well resolved.

Fig. 6 represents the evolution of NO_2 on the sensor surface in time. In red, the results for a time step of $3.77{\cdot}10^{-3}$ s are represented and in gray for a time step of $1.88{\cdot}10^{-3}$ s. It can be seen that there is a slight difference in the increment of NO_2 in the first 8 min. Then the results overlap obtaining the same evolution in time. Taking into account that the computational time for a time step of $3.77{\cdot}10^{-3}$ s using 12 cores in a 128 Gb RAM workstation was of around one month (with a time step of $1.8{\cdot}10^{-3}$ two months) the slight difference does not justify a smaller time step.

3.1.3. Results convergence study

For the thermal validation of the numerical model, the stationary temperature achieved on the sensor was evaluated. This temperature distribution was analyzed both numerically and experimentally. For the experimental determination of the temperature, a thermal camera (FLIR-P25) was used, after applying a power of 2 W to the heating resistor of the sensor. This is done in the CFD model where constant properties are assumed for the platinum used as heater material. The zone analyzed for the validation is focused on the X-axis along the sensor, which means that a length of around 5 mm is compared. In Fig. 7a is shown the experimental image analyzed and in Fig. 7b the numerical results of the temperature distribution.

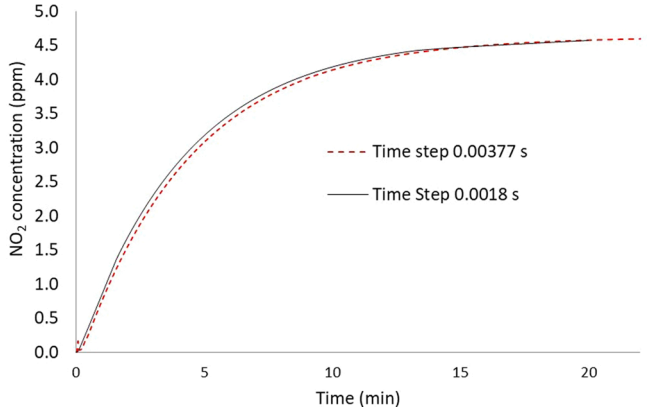

Fig. 6. Evolution of NO_2 concentration on the sensor surface in time at different time steps for Case I.

As is shown in Fig. 7 the temperature distributions are very close. In both cases, the temperature is concentrated on the chip area where the maximum temperature between models differs only on 0.07% in the middle of the sensor. In Fig. 8, the temperature distribution for both cases is represented in the X-axis, where 0 mm distance represents the center of the sensor, negative values and positive values of the distance represent the left side and the right side from the center of the sensor respectively. This great adjustment to the temperature distribution, confirms that the model is fully validated.

The slight variation between them can be due to the thin film used as sensitive material, with a thickness of 150 nm that is not represented in the CFD model. It could be the origin of the slight changes in the maximum temperature value and temperature distribution.

3.2. Comparison between numerical and experimental results

Four different cases were analyzed (both numerically and experimentally), corresponding to combinations of two different sensor assembly positions (bottom and middle of the chamber) and two different inlet flow rates (200 sccm and 400 sccm). See Table 1.

In Fig. 9, the simulated NO_2 concentration in the sensing area is analyzed and plotted for the four cases as a function of time. All cases show that the maximum NO_2 concentration does not reach 5 ppm, even if the NO_2 concentration inlet is set to 5 ppm. The concentration increases fast at the beginning and reaches 90% of the final plateau value (T90) in a shorter time (4.25 min) for the 400 sccm cases, while in the 200 sccm cases it takes longer to reach the stabilization (8.25 min). Analyzing the focused zone, where the initial evolution is zoomed (from t = 0 min to t = 0.5 min), for the cases with the sensor placed at the bottom (case I and case II), at the very beginning, the detected NO_2 concentration is null, as the flow does not reach sensor yet. Afterward, the evolution of the NO_2 concentration shows a peak up to 0.2–0.3 ppm, and afterward, the concentration increases with a smoother slope. For the cases where the sensor is placed is facing the inlet (case III and case IV), a sudden increase of NO_2 up to 1.5 ppm happens because the inflow impacts directly on the sensor. Once this jump in concentration occurs, there is a slight decrease and finally, the concentration increases with a smoother slope. On the whole, the evolution for the case of 400 sccm is faster and for all the cases, this evolution stabilizes at a *plateau* of 4.5 ppm of NO_2 as stated before. This could be a consequence of a double contribution, the geometry of the chamber where the inlet and outlet are at the same level and due to the convection flows that take place inside.

The experimental gas sensing velocity is plotted in Fig. 10, where the sensor response as a function of time is shown.

The response time of the sensor in all four cases is in line with the simulations time scale, showing a good agreement between the simulated and the experimental data. The sensor in the cases with 400 sccm shows the fastest response time of 5.3 min and 4.8 min for case II and case IV respectively. The longest response time among the tested situations is observed in case I (11.7 min), probably due to a combination of two facts, the lower flux and the bottom position. With the same flux and middle position (case III), the response time decreases down to 9.3 min

If the stationary value of the response is analyzed, the experimental data show that for both flow rates, the sensor at the "bottom" position gives a higher response than the sensor at the "middle" position. This could be explained by the fact that the higher velocity of the gas arriving at the sensor surface at the "middle" position, could have a cooling effect on the sensor surface, thus leading to a lower response.

If the stationary values of the responses at the same position are compared for the two flow rates, we see that at both positions the highest flow gives a higher stationary response. If we consider that in a certain position the temperature conditions will be comparable, and

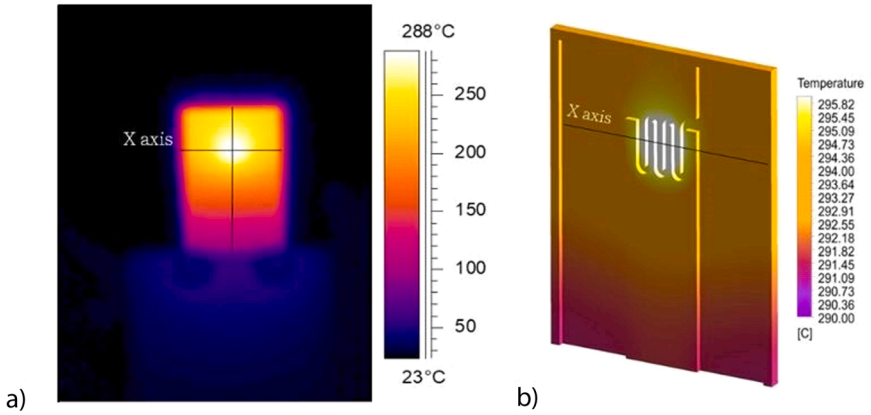

Fig. 7. Temperature distribution on the sensor where the compared X-axis is illustrated. a) Experimental results and b) numerical results.

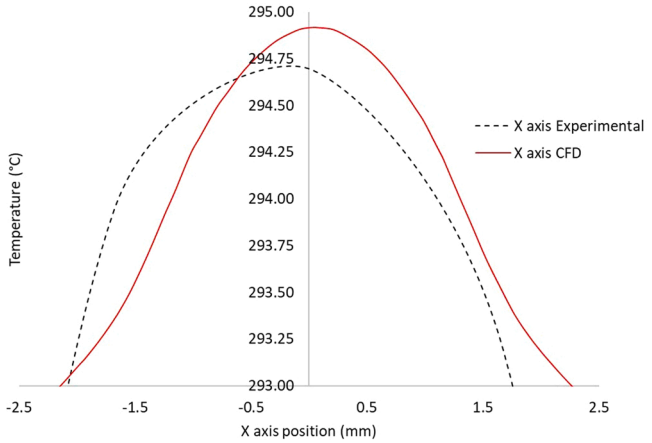

Fig. 8. Temperature distribution in the X-axis of the sensor area. In red CFD values and in dotted line the experimental results are represented.

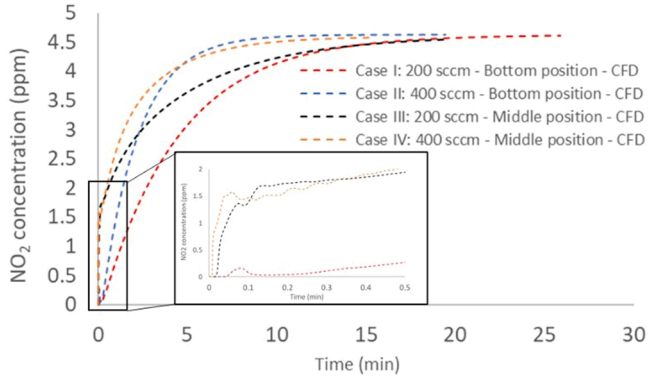

Fig. 9. Simulation results of the evolution of NO_2 concentration on the sensing area for the four cases analyzed. The zoomed area is show for time between T = 0 s and T = 0.5 s.

thus the reaction rate similar, then the higher response for higher flows could be explained because of the higher diffusion rate of the gas into the sensing material.

With the aim of comparing the evolution in time of both, numerical and experimental, the experimental results are normalized to the numerical ppm concentration. For this, the maximum Rg/Ra response is equated to the maximum ppm concentration in each case of the numerical results. As a conclusion the following two graphs are obtained, where bottom position (Fig. 11 a)) and middle position (Fig. 11 b)) cases

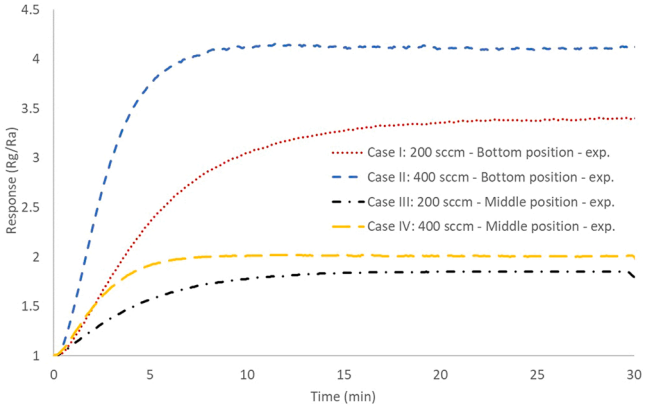

Fig. 10. Sensor response versus time for the four analyzed cases.

are compared separately for better visualization.

For cases at the bottom position, the NO_2 concentration vs time CFD results shows a higher slope at the beginning, than the experimental curve that gives the sensor response. The diffusion-reaction and transduction mechanisms that give rise to the final electrical response in the sensor require some time, so the difference in slopes between experimentally measured electrical response data and the CFD simulated NO_2 concentration would mean that the velocity of the response is slower than the velocity of the gas molecules arriving at the sensor surface. We can see that the difference between the curves at the beginning of the detection process is bigger at the middle position. If we consider that the reaction rate is similar (same gas and temperature), this would mean that the detection mechanism is diffusion-limited and that a higher concentration reaching the surface does not necessarily mean a faster response, because a diffusion time is needed to measure a change in resistance in the electrodes below the sensing material. But a second consideration can be made: at the middle position, the gas flow reaching the surface can induce a decrease in the surface temperature, thus a slower reaction rate, which would mean also that after the gas molecule reaches the sensor surface, it needs a longer time to react and thus give an electrical response.

To do a deeper numerical results analysis, an arbitrary time was analyzed. As the results are time-dependent, an arbitrary fixed NO_2 mass quantity inlet in time was fixed. The arbitrary time for the evaluation was fixed to 100 s for an inlet flow rate of 400 sccm, which means that for the case of 200 sccm, the time evaluated is 200 s

Fig. 12 and Fig. 13 show the numerical simulation results. In both figures in the left part (a and c), the sensor is placed in the bottom position, while in the right (b and d) is placed in the middle position. In the top part (a and b) the flow rate is 200 sccm and in the bottom (c and d) is

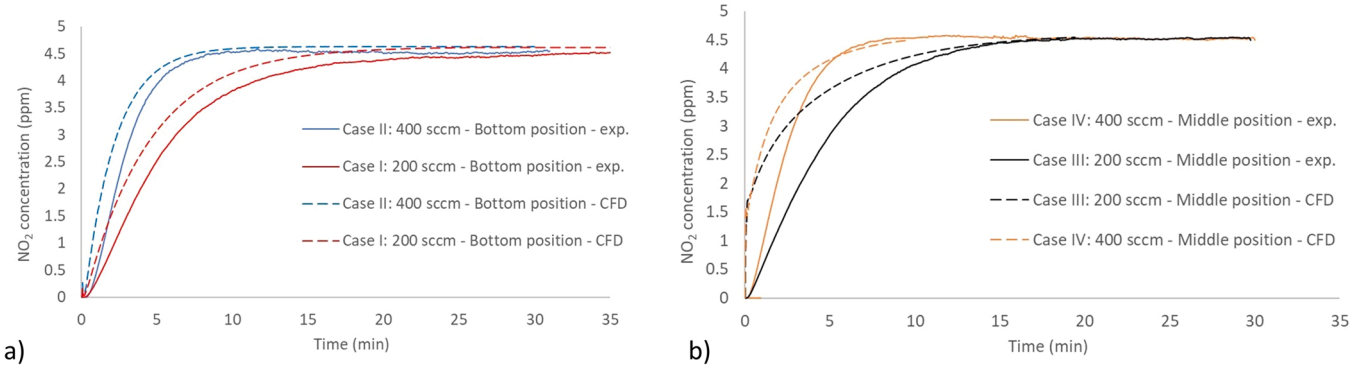

Fig. 11. NO_2 concentration evolution numerical – experimental comparison. a) sensor placed at bottom position cases (case I and case II) and b) sensor placed at middle position cases (case III and case IV).

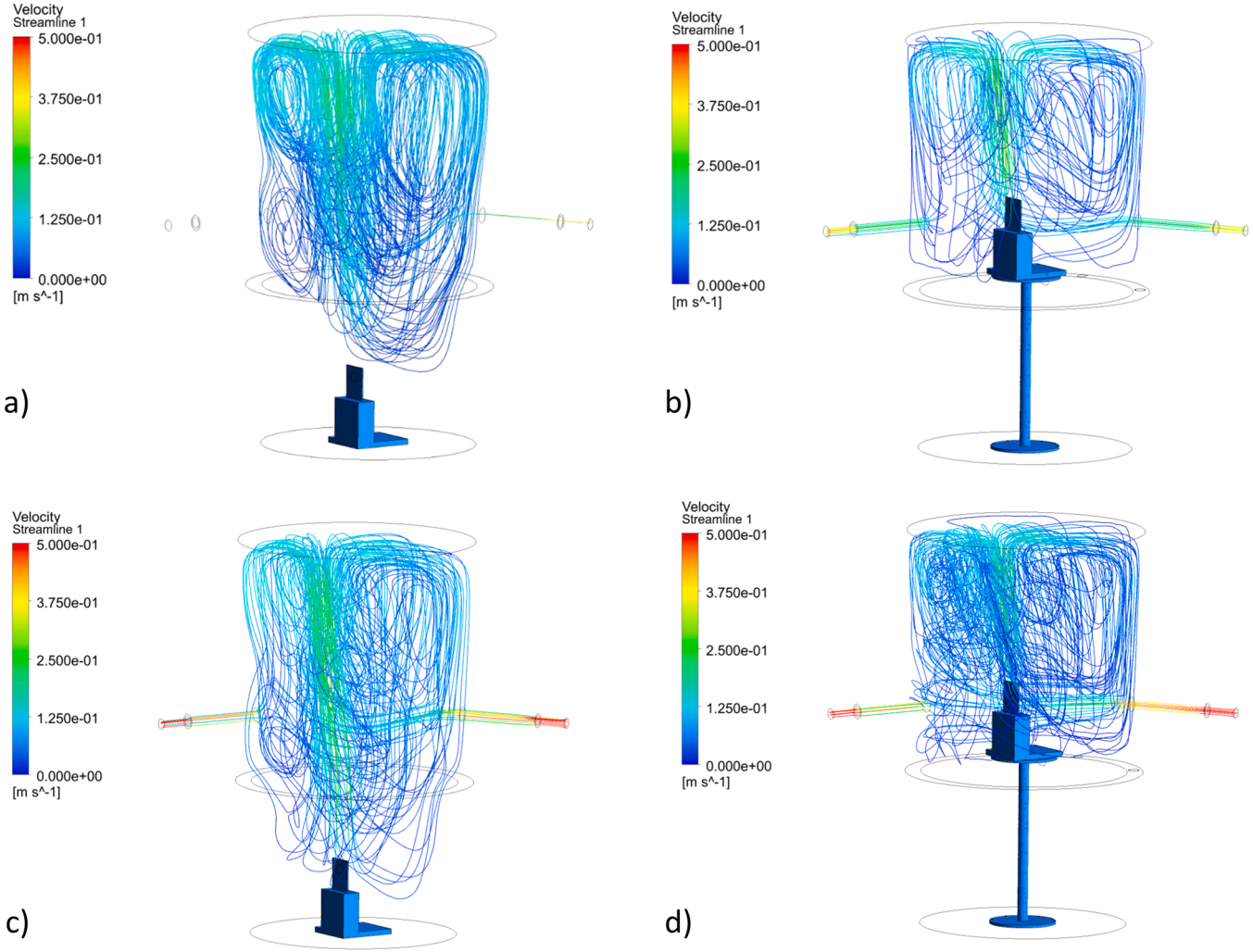

Fig. 12. Streamlines where color represents the velocity (blue minimum, red maximum). a) Case I b) case III, c) case II and d) case IV).

400 sccm. Fig. 12 shows the streamlines for each case, where the color is representative of the velocity.

In Fig. 13 the mass fraction of NO_2 is plotted as a volume rendering (where the blue and red color corresponds to the minimum and maximum mass fraction of NO_2 respectively). In zebra color velocity volume rendering is illustrated.

As can be seen in Fig. 12, for the cases where the sensor is placed in the middle position, the streamlines of the flow are concentrated in the top middle part, while for the cases with the sensor placed in the bottom, the distribution is more homogeneous in the chamber. These differences in the streamlines have a big impact on the distribution of the NO_2. Notice how in Fig. 13 for cases where the sensor is placed in the middle position, the NO_2 is concentrated in the middle top part. This effect can be explained by the convection fluxes. The distribution of convection in the volume of the chamber is controlled by the boundary conditions, the position of the sensor and the geometry of the chamber. In addition, the

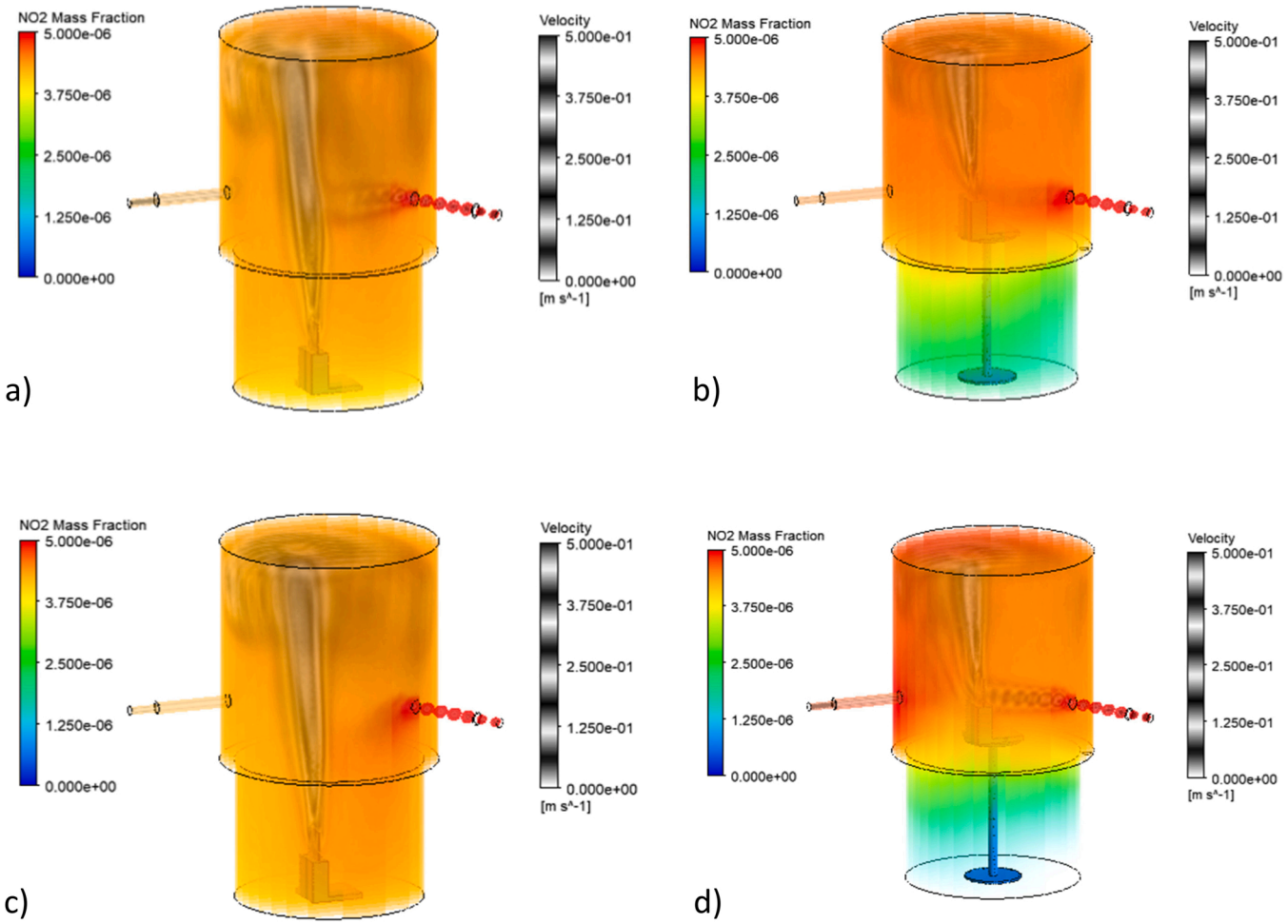

Fig. 13. Volume rendering of NO_2 concentration where red represents the maximum concentration and blue the minimum. In zebra color, the velocity is illustrated. a) Case I b) case III, c) case II and d) case IV).

magnitude of the convection is enhanced by the heat source of the sensor as the velocity illustration shows in Fig. 13. For the cases with the sensor in the bottom position, the dominant convection fluxes start in the sensor, travel up to the top part, and finally travel close to the walls up to the bottom part, generating a loop. This movement generates a homogeneous distribution of the NO_2 in the whole chamber. For the cases where the sensor is placed in the middle position, the convention fluxes do not travel till the bottom part. Due to the big ascendent velocity of air from the heat source of the sensor, this convention flux, closes the loop in the middle of the chamber, increasing the NO_2 concentration in the middle top part of the chamber. This effect is well reproduced in the experimental NO_2 time evolution, where for the cases at the bottom position the concentration *plateau* is reached several minutes after as shown in Fig. 11.

These simulation results confirm the relevance of the position of the sensor, the inlet flow and the geometry of the test chamber itself in the fluid dynamics on the surface of the sensor, and thus on the gas concentration reaching the sensor surface. Moreover, according to the numerical results, the position of the heat source (sensor heater on the chip) also influences the distribution of the chemical specimen (NO_2 in this case) due to the convective flow originated by thermal effects, and thus, on the gas concentration reaching the sensor surface. Taking this fact into account, it is concluded that the response time depends highly on these variables and special care must be taken when characterizing it.

As already known and demonstrated by the results, a small chamber as well as a high gas flow to carry out the experiments improve both the response and recovery time of gas sensing devices. Therefore, before setting up a new experiment, it would be optimal to use one of the smaller chambers that your sensor device allows as well as the highest gas flow available in the laboratory. Once this is defined, as shown in this article, in order to minimize artifacts due to the chamber shape, sensor position and gas flow, it would ideal to first perform CFD simulations of the setup (chamber and sensor dimensions and gas characteristics) with the sensor at different possible positions and temperatures to verify which is the optimal position where the maximum concentration of gas arrives faster to the sensitive material.

4. Conclusions

As shown in the results, the simulations of the temperature distribution on the sensor surface match the experimental data measured by the IR thermographic camera. This demonstrates the utility of the simulation tool to design a heating device according to the desired temperature distribution.

The experimental results on the sensor response show a qualitative good correlation with the evolution of the concentration gradient given by the CFD simulations. Therefore, the use of this approach allows the optimization of the design of test chambers, both for experimental purposes and also with the view of practical detector devices, in which the flow conditions could be set for the optimized detection of the target gases.

The simulation results demonstrate that the convective fluxes generated inside the chamber are a key parameter on the gas concentration distribution captured by the sensor surface. Thus, the position,

the geometry and the inlet-outlet conditions together with the temperature gradient generated by the sensor, have a big impact on the response time evolution.

From those results, it can be also concluded that the comparison of response and recovery time among the different gas sensors reported in the literature is a complicated task, especially when no CFD simulations have been carried out since it is hard to dissociate the real response/recovery time of the sensor itself and the time that the gas takes to reach the sensitive surface due to the chamber size, sensor temperature and gas flow. Moreover, the presented approach of comparing the simulated evolution gas concentration on the sensor surface with the experimental sensor dynamic response can be used as a tool to evaluate the real response time of a sensor, by comparing the difference in the evolution of the two curves.

CRediT authorship contribution statement

L. Parellada MonrealX Conceived and designed the analysis, X Collected the data, X Performed the analysis, X Wrote the paper. G. García Mandayo X Conceived and designed the analysis, X Collected the data, X Performed the analysis, X Wrote the paper. A. Martín-Mayor X Conceived and designed the analysis, X Contributed data or analysis tools, X Performed the analysis, X Wrote the paper. I. Souto-CanteliX Conceived and designed the analysis, X Contributed data or analysis tools, X Performed the analysis, X Wrote the paper. M. Mounir Bou-Ali X Conceived and designed the analysis, X Contributed data or analysis tools, X Performed the analysis, X Wrote the paper.

Declaration of Competing Interest

The authors declare that they have no known competing financial interests or personal relationships that could have appeared to influence the work reported in this paper.

Acknowledgments

Mondragon Goi Eskola Politeknikoa (MGEP) and Ceit thank Elkartek Project KK-2021/00082 (micro4IloT) and IT1505-22 (Research Group Program) of the Basque Country Government for funding the research activities in this paper.

References

[1] J.T.W. Yeow, Y. Wang, A review of carbon nanotubes-based gas sensors, J. Sens. (2009) (2009), https://doi.org/10.1155/2009/493904.
[2] T. Wang, D. Huang, Z. Yang, S. Xu, G. He, X. Li, N. Hu, G. Yin, D. He, L. Zhang, A review on graphene-based gas/vapor sensors with unique properties and potential applications, Nano Micro Lett. 8 (2016) 95–119, https://doi.org/10.1007/s40820-015-0073-1.
[3] W.-T. Koo, J.-S. Jang, I.-D. Kim, Metal-organic frameworks for chemiresistive sensors, Chem 5 (2019) 1938–1963, https://doi.org/10.1016/j.chempr.2019.04.013.
[4] F.-E. Annanouch, G. Bouchet, P. Perrier, N. Morati, C. Reynard-Carette, K. Aguir, M. Bendahan, How the chamber design can affect gas sensor responses, Proceedings 2 (2018) 820, https://doi.org/10.3390/proceedings2130820.
[5] L. Lopez, V. Copa, T. Hayasaka, M.A. Faustino-Lopez, Y. Wu, H. Liu, Y. Liu, E. Estacio, A. Somintac, L. Lin, A. Salvador, Influence of chamber design on the gas sensing performance of graphene field-effect-transistor, SN Appl. Sci. 2 (2020), https://doi.org/10.1007/s42452-020-2676-5.
[6] F. Yaghouti Niyat, M.H.Shahrokh Abadi, COMSOL-based modeling and simulation of SnO2/rGO gas sensor for detection of NO2, Sci. Rep. 8 (2018) 1–12, https://doi.org/10.1038/s41598-018-20501-2.
[7] L. Parellada-Monreal, S. Gherardi, G. Zonta, C. Malagù, D. Casotti, G. Cruciani, V. Guidi, M. Martínez-Calderón, I. Castro-Hurtado, D. Gamarra, J. Lozano, L. Presmanes, G.G. Mandayo, WO3 processed by direct laser interference patterning for NO2 detection, Sens. Actuators B Chem. 305 (2020), 127226, https://doi.org/10.1016/j.snb.2019.127226.
[8] J. Bardina, P. Huang, T. Coakley, Turbulence Modeling Validation, Testing, and Development Physics, 1997.
[9] ANSYS Fluent Theory Guide, ANSYS, Inc, Southpointe 2600 ANSYS Drive Canonsburg, PA 15317,2020.
[10] W.J. Massman, A review of the molecular diffusivities of H2O, CO_2, CH4, CO, O3, SO2, NH3, N2O, NO, and NO2 in air, O2 and N2 near STP, Atmos. Environ. 32 (6) (1998) 1111–1127.
[11] F.R. Menter, Zonal two equation k-w turbulence models for aerodynamic flows, Physics (1993), https://doi.org/10.2514/6.1993-2906.

Dr. L. Parellada-Monreal received her BSc degree in Physics from the University of Barcelona in 2013 and her MSc degree in Nanophysics and Nanostructures from the University Joseph Fourier in Grenoble in 2015. In 2019 she received her Ph.D. in Applied Engineering (University of Navarra, Spain) focused on semiconductor nanostructured materials for gas sensing applications for NO2 detection. Since then she has been working on gas and light-sensing devices. Currently, she is a post-doc researcher at the Fondazione Bruno Kessler in Trento (Italy) working on the development of 3D-integration of Silicon Photomultipliers (SiPMs) for high energy physics experiments and medical applications. She is the author or co-author of 11 publications and conference papers.

Prof. G. García Mandayo (Ph.D., female) is a Researcher and Project Manager in the Materials and Manufacturing Division of Ceit-BRTA and Professor of the Electrical and Electronic Engineering Department of the University of Navarra. She obtained her Degree in Electronics Engineering (1996) and her Doctorate (2002) from the University of Navarra. Her main research and technical interests are in the field of materials fabrication and development applied to functional surfaces, such as sensing devices, and in the use of laser technology for the modification of the material surface properties. She has participated in more than 40 national and international research projects, leading at least 17 of them. She is an active referee of significant scientific publishing houses and evaluator of scientific projects for public agencies such as ANEP in Spain and the European Commission. She is also the vice-president of the Spanish Chapter of the IEEE Sensors Council.

Dr. A. Martin-Mayor: Ph.D. in Engineering from Mondragon Unibertsitatea (Mondragón, Spain, 2012). He has developed his research activity during his training period in the area of Fluid Mechanics, where he is currently pursuing his research career. His multidisciplinary experience in laboratory techniques, design and development of experimental devices (with two patents in this field), characterization of complex fluids (a patent in this field), as well as in numerical simulation of thermofluidic processes, mixing/separation processes and in microfluidics, oriented to biotechnological and industrial interest, is highlighted. He has published 9 papers in scientific journals in the field of micro/nanofluidics and has participated in more than 20 international conferences. Since 2012 he is lecturer at Mondragon Unibertsitatea on topics related to automation, fluid mechanics and microfluidics, so he has solid knowledge in sensorization, in the assembly and experimentation of pneumatic and hydraulic circuits.

I. Souto-Canteli is a lecturer and researcher in Fluid Mechanics at MGEP (Basque Country, Spain). He obtained his first degree in Mechanical Engineering at Basque Country University in 2015. He holds an MSc in Renewable Engineering from Basque Country University. After three years of consultory services at a computational dynamic fluid simulation company in Austria, he started working in the Fluid Mechanics group at MGEP and started his Ph.D. in phase change cooling techniques for battery pack optimization.

Prof. M. Mounir Bou-Ali received his Ph.D. in Physics (UPV / EHU, 1999). He has developed his research during his research in the areas of Fluid Mechanics and transport phenomena. Since 2002, he has been teaching at the University of Mondragon, with research in fluid mechanics activity, being the coordinator of the line of R & D in Fluid Mechanics. He is currently developing his research on issues related to transport phenomena in liquid mixtures; synthesis, characterization and analysis of magnetorheological fluids, as well as the development of new methods of separating in micro-biotechnological. He has published over 150 papers in scientific journals, book chapters, international and national conferences and has made 12 patents. He has also directed 10 doctoral theses and has led more than 40 national and international projects. For his part, he has organized various international events such as the international congress on thermodiffusion (IMT7–2006) and the Benchmark on the Soret effect in multicomponent mixtures (2015). In recent years he has participated, as a scientist, in various spatial experiments of microgravity. Since 2010, he has been part of the "Thematic Team: Liquid Diffusion", established by ESA to coordinate the DCMIX experiment (Diffusion and thermodiffusion in ternary mixtures) that is currently explained in the European module of the ISS. In 2015, the scientific team of the SCCO-SJ10 experiment has been incorporated, which has been followed by experimental measurements at high pressures in 2016 aboard the Chinese space capsule Shijian 10. Currently, Prof. M. Mounir Bou-Ali is coordinating the fourth DCMIX4 mission is analyzed under microgravity conditions for the multicomponent mixture of nanofluids.